Strain-induced magnetic order in RuO_2 from first-principles calculations

Wending Liu,[1,*] Xiaoyu Feng,[1,2,*] Jun Zhao,[1] Peng Zhang,[3] Dangwei Guo,[1] Desheng Xue,[1] Mingsu Si,[4] ZhenHua Li,[5,6,7,8] Fangjun Guo,[9] and Xiaolong Fan[1,†]

[1]*The Key Laboratory of Magnetism and Magnetic Functional Materials of Ministry of Education, Lanzhou University, Lanzhou 730000, China*
[2]*State Key Laboratory for Artificial Microstructure & Mesoscopic Physics and Frontiers Science Center for Nano-Optoelectronics, School of Physics, Peking University, Beijing 100871, China*
[3]*Xi'an Microelectronics Technology Research Institute, Xian 710025, China*
[4]*School of Materials and Energy, Lanzhou University, Lanzhou 730000, China*
[5]*Lanzhou Center for Theoretical Physics, Lanzhou University, Lanzhou 730000, China*
[6]*Key Laboratory of Theoretical Physics of Gansu Province, Lanzhou University, Lanzhou 730000, China*
[7]*Key Laboratory of Quantum Theory and Applications of MoE, Lanzhou University, Lanzhou 730000, China*
[8]*Gansu Provincial Research Center for Basic Disciplines of Quantum Physics, Lanzhou University, Lanzhou 730000, China*
[9]*Lanzhou Institute of Physics, Lanzhou 730000, China*

(Received 31 January 2026; revised 2 August 2026; accepted 11 August 2026; published 16 September 2026)

RuO_2, proposed as a potential altermagnet, is expected to serve as a new-generation spintronic material enabling precise control of spin transport. However, the existence of magnetic order in RuO_2 has recently been widely questioned. Here, based on first-principles calculations, we systematically investigate the magnetic order in RuO_2 under epitaxial strain. We find that a modest global strain can drive RuO_2 from a nonmagnetic state to an antiferromagnetic state. Furthermore, near the strain-induced magnetic critical point, a modest local distortion can stabilize a spin-density-wave state over the antiferromagnetic state, with an energy difference on the order of 10−100 μeV and a characteristic wavelength of about 7–10 nm. Our study provides a unified microscopic picture for the experimental controversy regarding altermagnetism in RuO_2, and highlights the key roles of global strain and local distortion in tuning RuO_2 magnetism and spin transport.

DOI: 10.1103/4gky-vck5

I. INTRODUCTION

In recent years, research on altermagnetism has developed rapidly. Altermagnets exhibit no net magnetization in real space, but owing to the rotational crystal symmetry, they can host a pronounced spin splitting in momentum space. Therefore, altermagnets combine some features of both ferromagnets and antiferromagnets, thus attracting considerable attention in the field of spintronics. In this context, the prediction of a large spin-splitting energy and a high Néel temperature in RuO_2 [1], together with theoretical groundwork [2–4] and rapid experimental progress on the altermagnetic spin-splitting effect [5], have jointly propelled RuO_2 to become a research hotspot in altermagnetism.

But, in recent years, many experiments have supported RuO_2 being closer to a Pauli-paramagnetic metal instead of an altermagnet: μSR results indicate the absence of observable internal dynamic magnetic fields and long-range magnetic order [6,7]. Some ARPES measurements also show a band structure more consistent with a nonmagnetic (NM) state [8,9]. Quantum oscillation experiments pose an even stronger challenge to the existence of antiferromagnetic (AFM) order [10]. But at the same time, several works have emphasized that the magnetism of RuO_2 is intrinsically fragile. For instance, the relatively small Fermi velocity near the Fermi surface makes its magnetism highly susceptible to external perturbations [11,12]. Accordingly, it has been proposed that extrinsic factors may play an important role in the magnetic order of RuO_2, such as oxygen vacancies, epitaxial strain, and symmetry breaking at interfaces [11,13,14]. Moreover, it has been reported that tuning the electron count via electron-type or hole-type impurities can modify the Néel-vector orientation and enhance the experimental signatures of antiferromagnetism [15,16]. But in bulk RuO_2, these external factors are relatively weak, which instead lead to a weaker magnetic order compared to the RuO_2 thin film [17]. These results further highlight the critical impact of extrinsic effects on RuO_2.

Building on these considerations, a growing number of studies have begun to focus on how strain modifies the magnetism and electron transport in RuO_2 [18–20]. Some experiments have also started to explore fine control of substrate–film coupling via the film thickness [21,22]. Application-oriented studies have further proposed using epitaxial strain to control the details of spin transport in RuO_2, thereby expanding the tuning dimension for spintronic devices [13,23]. However, obtaining a direct physical picture of how strain influences magnetism in RuO_2 by experiments remains challenging. First, in most cases, strain is imposed via the substrate, which also introduces other contributions, such as interlayer spin-orbit coupling (SOC), interlayer

*These authors contributed equally to this work.
†Contact author: fanxiaolong@lzu.edu.cn

TABLE I. The lattice constants used in the paper.

	No SOC		SOC	
	RuO_2	TiO_2	RuO_2	TiO_2
a (Å)	4.520636	4.651569	4.520430	4.649642
c (Å)	3.126933	2.969593	3.120534	2.969468

exchange coupling and interlayer spin reorientation [24]. These complications increase the difficulty of data interpretation and restrict the strain tuning range. Second, most instruments do not allow the strain tuning during magnetic measurements, so it is difficult to establish a systematic and comprehensive strain-magnetism relationship in RuO_2. In contrast, first-principles calculations can largely eliminate other effects and directly address the influence of strain on the magnetism of RuO_2, while being subject to fewer practical constraints than experiments. Therefore, the first-principles calculations can provide a feasible and valuable route to obtain initial microscopic understanding of strain-induced magnetic order in RuO_2.

Using the widely studied system of RuO_2 epitaxially grown on TiO_2 substrates as an example, we approximate the substrate effect as the strain applied to the RuO_2 lattice. We systematically investigate how global strain and local distortions affect the magnetism of RuO_2. Results show that even without using the still-debated DFT + U treatment, RuO_2 can undergo a transition from a nonmagnetic state to an antiferromagnetic state once the global strain reaches a certain level. Furthermore, when the local distortion reaches a modest level, the spin-density-wave (SDW) state may become energetically more favorable than the AFM state. These results provide a consistent microscopic picture for the rich extrinsic magnetism of RuO_2 and clarify the strain-induced magnetic order in RuO_2.

II. COMPUTATIONAL METHOD

Our first-principles calculations were performed using the VASP package within the framework of density functional theory (DFT). Perdew-Burke-Ernzerhof (PBE) exchange–correlation functional was adopted, and the interaction between valence electrons and ionic cores was described using the corresponding pseudopotentials [25–30]. The valence configurations were treated as Ru_pv ($4p^6 4d^6 5s^1$), O ($2s^2 2p^4$), and Ti_pv ($3p^6 3d^3 4s^1$). The plane-wave energy cutoff was set to 520 eV. We used the Methfessel-Paxton method with a width of 0.15 eV. The lattice constants of RuO_2 and TiO_2 employed in this work are listed in Table I.

For calculations of the unit cell, the Brillouin zone was sampled using a Γ-centered 9 × 9 × 13 k-point mesh. For supercells expanded along the a axis, a Γ-centered 1 × 9 × 13 k-point mesh was adopted, and the DOS was computed using a 2 × 18 × 26 k-point mesh.

All magnetic calculations in the main text were obtained from standard self-consistent collinear spin-polarized calculation [except the SOC results in Fig. 1(b)]. Also, we have added the robustness tests of our calculation results to different input parameters in Supplemental Material S8 [31]. These calculation results ensure that our conclusion remains correct in different computing conditions.

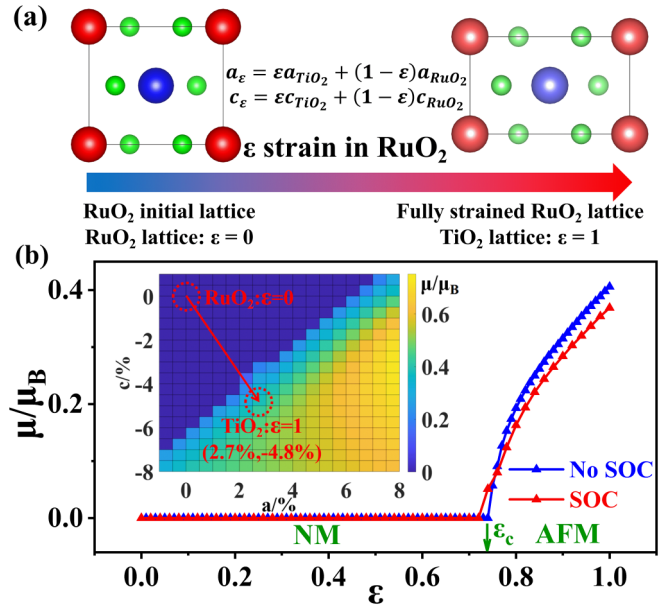

FIG. 1. Global strain induced RuO_2 magnetic order by TiO_2 substrate. (a) Schematic illustration of the global strain applied to RuO_2. (b) Evolution of the magnetic moment of RuO_2 as a function of ε, showing a transition from a nonmagnetic state to an antiferromagnetic state when $\varepsilon \approx 0.74$. The mapping plot shows the results under strain in RuO_2.

For structural convergence, the ionic relaxation criterion for the unit cell calculations was 0.001 eV/Å. To control the computational cost while maintaining accuracy, we required the force on O atoms to be within 0.05 eV/Å in supercell calculations. The rationale for the threshold of the relaxation criterion, together with comparisons to more stringent relaxation settings and the methodology used, is provided in the Supplemental Material S1 [31].

To avoid possible misunderstanding, we will use the term antiferromagnetism rather than altermagnetism to describe the magnetism of RuO_2 in the main text, except in the discussion of Fig. 3. This is because the present work focuses primarily on magnetic compensation rather than on the distinctive properties of altermagnetism.

In Sec. III B, we use AFM and SDW to distinguish two different magnetic configurations. Here, AFM refers to a magnetic configuration in which the Néel vector does not change its direction within the supercell, whereas SDW refers to a configuration in which the Néel vector reverses its direction once within the supercell. In the calculation comparing AFM with SDW, no magnetic constraint is imposed on the magnetic moments. The only difference in calculation lies in the choice of the initial magnetic moments. For the SDW state, it is necessary to reflect the change of the Néel vector direction with space [32]. At the same time, we ruled out the possibility of the helical state in Sec. III B, because the helical state would automatically evolve into the SDW state.

Data postprocessing and visualization were mainly carried out using VESTA and VASPKIT [33,34]. The main-text results are primarily based on calculations without SOC and

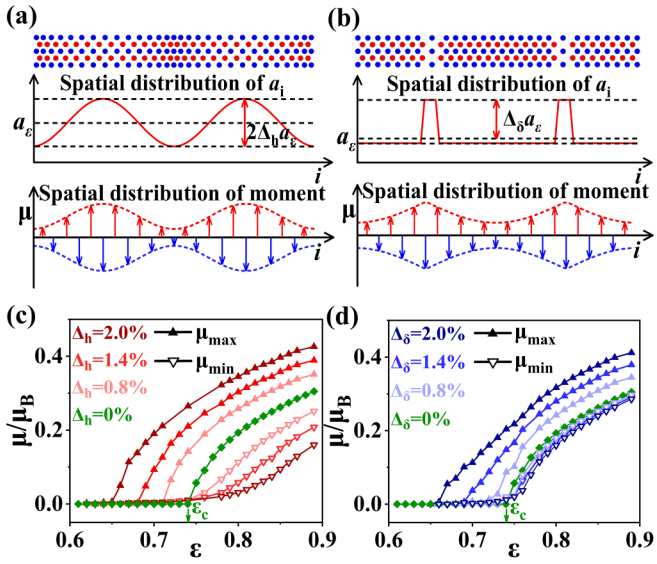

FIG. 2. The magnetic order in RuO_2 considering both global strain and local distortions. (a), (b) Schematic diagram of the spatial distribution of lattice constant and magnetic moment distribution under (a) harmonic distortion and (b) δ-type distortion. (c), (d) Variation of μ_{max} and μ_{min} with global strain ε when $n = 9$ under (c) harmonic distortion and (d) δ-type distortion.

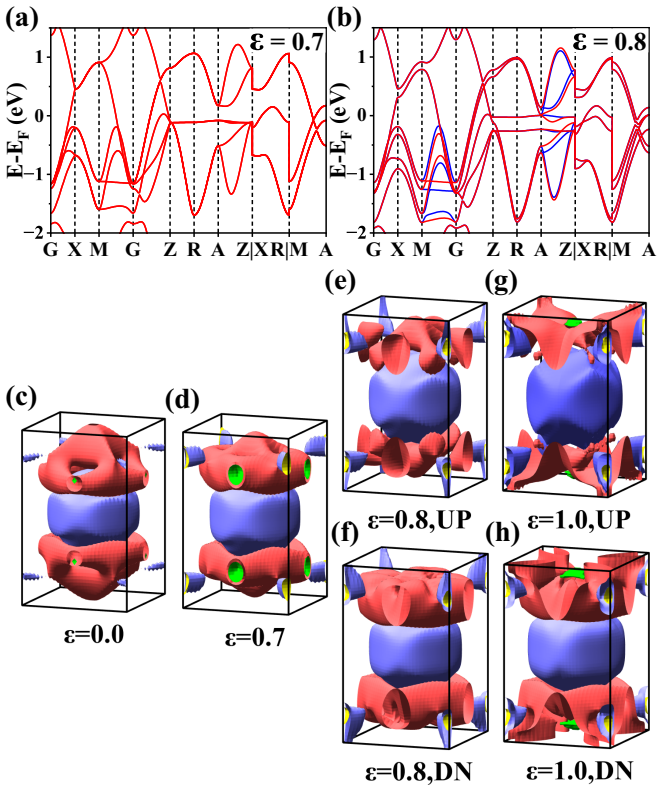

FIG. 3. (a), (b) The band structure of RuO_2 when (a) $\varepsilon = 0.7$, (b) $\varepsilon = 0.8$. (c)–(h) The Fermi surface structure of RuO_2 when (c) $\varepsilon = 0.0$, (d) $\varepsilon = 0.7$, (e) $\varepsilon = 0.8$, UP, (f) $\varepsilon = 0.8$, DN, (g) $\varepsilon = 1.0$, UP, (h) $\varepsilon = 1.0$, DN. Different colors are used to distinguish Fermi surface sheets originating from different bands.

DFT + U. Comparisons and additional analysis involving SOC and DFT + U are presented in Supplemental Material S2 and S3 [31].

III. RESULTS AND DISCUSSION

A. RuO_2 magnetic order under global strain

RuO_2 is a strain-sensitive material. The fragility of its Fermi-surface structure makes its magnetism susceptible to strong modulation by lattice strain. TiO_2 and RuO_2 both have a rutile structure and their lattice constants are well matched, which means that RuO_2 single crystal is easy to epitaxially grow on TiO_2 substrate. Therefore, it is natural to discuss strain-induced magnetic order in RuO_2 by taking TiO_2 substrate strain as a starting point. To quantify the global strain effect of the TiO_2 substrate on epitaxial RuO_2 thin films, we introduce a global strain parameter ε. It describes the degree to which the RuO_2 lattice is continuously strained from its intrinsic lattice toward that of TiO_2 [Fig. 1(a)]. When $\varepsilon \to 0$, the lattice constants approach the intrinsic RuO_2 values; when $\varepsilon \to 1$, the lattice constants approach the intrinsic TiO_2 values. The lattice constants are defined as follows:

$$a_\varepsilon = \varepsilon a_{TiO_2} + (1-\varepsilon)a_{RuO_2},$$
$$c_\varepsilon = \varepsilon c_{TiO_2} + (1-\varepsilon)c_{RuO_2}. \quad (1)$$

In a RuO_2 unit cell, there are two Ru atoms which are the same in magnetic moment magnitude but opposite in direction. The variation of the magnetic moment value with ε is shown in Fig. 1(b). With increasing ε, the system can undergo a transition from a nonmagnetic state to an antiferromagnetic state. A finer scan yields a critical strain $\varepsilon_c = 0.7404$ (without SOC) for the RuO_2 unit cell. Upon including SOC, the critical point shifts slightly to $\varepsilon_c = 0.7340$, indicating that the conclusion above is not qualitatively altered by SOC. The main difference lies in the moment magnitude. For $\varepsilon > \varepsilon_c$, SOC reduces the moment by about 10% compared with the No-SOC results. Therefore, in the following we primarily discuss the results without SOC. Also, the above discussion also applies to the slab model. However, due to interface effects, the critical global strain ε required to produce magnetic order at the interface is smaller, which may have a subtle effect on the magnetism of RuO_2 surface (more details are shown in Supplemental Material S6 [31]).

Substrate-induced lattice strain is not unique to RuO_2 epitaxially grown on TiO_2. It is also commonly encountered for other substrates such as MgF_2 and Al_2O_3 [35]. Considering the intrinsic magnetic fragility of RuO_2, some local structural imperfections may also affect the magnetic order in RuO_2, such as substrate–film heterojunction, epitaxial defects, interfacial effects, and local relaxations. Therefore, describing the realistic film system solely by a global strain parameter ε is insufficient. ε only captures the global strain but misses local details. Accordingly, we also introduce the local distortion to examine the effect of local structural imperfections in the magnetic order of RuO_2. Specifically, we construct $n \times 1 \times 1$ supercells by expanding RuO_2 unit cell along the (100) direction, where n denotes the local distortion period measured in the number of unit cells. Within the supercell, we keep $b = a_\varepsilon$ and $c = c_\varepsilon$ fixed and apply a prescribed modulation

only to the lattice constant a in each unit cell as a function of the unit-cell index i ($i = 1, 2, \ldots, n$) [Figs. 2(a) and 2(b)]. We consider two types of local-distortion models: harmonic distortion and δ-type distortion. For the harmonic case, the distortion has the period n and forms a spatially periodic modulation within the supercell, with Δ_h denoting the amplitude of the harmonic local distortion. The periodicity of the harmonic function ensures that ε remains unchanged, making it an idealized model that is convenient for understanding generic effects of smooth strain fluctuations [Fig. 2(a)]. For the δ-type case, the distortion also has the period n, but the lattice constant a varies in a δ function like manner within the supercell. Δ_δ characterizes the relative amplitude of the most tensile cell, while the remaining unit cells provide compensating compressions so ε is conserved [Fig. 2(b)]. The δ-type case is useful for mimicking situations with strongly localized distortions in thin films. The lattice-constant constructions for these two models are given by

Harmonic distortion:

$$a_i = a_\varepsilon\left(1 - \Delta_h \cos\frac{(2i-1)\pi}{n}\right),$$
$$b = a_\varepsilon, \quad c = c_\varepsilon, \tag{2}$$

δ–type distortion:

$$a_i = \begin{cases} a_\varepsilon(1+\Delta_\delta) & i = 1 \\ a_\varepsilon\left(1 - \frac{\Delta_\delta}{n-1}\right) & \text{otherwise,} \end{cases}$$
$$b = a_\varepsilon, \quad c = c_\varepsilon. \tag{3}$$

Considering that local distortions affect the lattice constants differently at different positions, the Ru magnetic moments vary with the position [Figs. 2(a) and 2(b)]. We note that the Ru moment increases with tension and decreases with compression, implying that tension favors the magnetic order while compression suppresses the magnetic order. In the following, we use the maximum moment $\mu_{\max}$ and the minimum moment $\mu_{\min}$ to characterize the magnetism of RuO_2. We set $n = 9$ to systematically examine the effects of ε and Δ_h on magnetic order. As shown in Fig. 2(c), under harmonic distortion, as Δ_h increases from 0.8%, 1.4%, to 2.0%, ε required for magnetism in the most tensile region (defined by $\mu_{\max} > 0.01\mu_B$) decreases slowly from 0.74 to approximately 0.72, 0.69, and 0.66. Meanwhile, the moment at the most compressed position is nearly zero for $\varepsilon < \varepsilon_c$ but begins to increase rapidly for $\varepsilon > \varepsilon_c$. (The magnetic moment when $\Delta_h = 0\%$ can be compared with $\mu_{\max}$ and $\mu_{\min}$ to discuss the influence of tension and compression on the magnetic order.) The calculation results in Fig. 2(c) indicate that ε plays the dominant role in controlling the global magnetic order: For systems with different local distortions, ε still needs to approach the vicinity of ε_c to establish global magnetic order. The presence of local distortion leads to different degrees of magnetism in different regions; specifically, the tensile region is more likely to develop magnetism under a smaller strain than the compressed region. Hence, a single critical global strain is not well defined, and we should describe a finite global strain window for the development of RuO_2 magnetic order. This window is ultimately modulated by ε_c, whereas its width is determined by the local distortion amplitude.

When the δ-type distortion is adopted, for $\Delta_\delta = 0.8\%$, 1.4%, and 2.0%, ε required for magnetism at the most tensile position are approximately 0.73, 0.70, and 0.67, respectively [Fig. 2(d)]. The moment at the most compressed position remains nearly zero for $\varepsilon < \varepsilon_c$ and starts to increase rapidly for $\varepsilon > \varepsilon_c$, in close agreement with the harmonic distortion results. Although the spatial distribution of the δ-type distortion differs substantially from that of the harmonic distortion, it yields similar ε required for magnetism at the most tensile position for the same amplitude parameter. (Part of the magnetic moment distributions are provided in Supplemental Material S4 [31].) Moreover, its global magnetic order also shows a strong dependence on ε.

Based on the systematic calculations of the global strain and the local distortion, our main results can be summarized as follows:

(1) The magnetic structure of RuO_2 is highly sensitive to the global strain; when the global strain reaches a certain level, the system undergoes a transition from a nonmagnetic state to an antiferromagnetic state. This conclusion remains unchanged after including SOC.

(2) For a given global strain, the local distortion can modulate the spatial distribution of the magnetic moment to some extent; however, whether the global magnetic order exists is still primarily controlled by global strain.

However, in an actual $TiO_2//RuO_2$ system, the magnetism of RuO_2 also depends on several factors, including film orientation, thickness, interface, and strain relaxation. And the strain cannot be determined solely by ε. Therefore, the discussion in the main text may not fully capture the complexity of the real heterostructure. But previous DFT studies on $TiO_2//RuO_2$ systems have shown that, under different conditions, RuO_2 can exhibit either antiferromagnetic or nonmagnetic behavior [21,36]. Moreover, in our calculations, the critical strain corresponds to lattice-constant changes of approximately 2.1% along the a axis and 3.5% along the c axis, which are comparable to the experimentally reported lattice variations in RuO_2 (more details are shown in Supplemental Material S10) [31,37–40]. Therefore, the TiO_2 substrate may drive RuO_2 into an antiferromagnetic or near-critical state, while in other cases it may allow RuO_2 to remain nonmagnetic. These results demonstrate the diversity of magnetism and magnetic instability in RuO_2. Therefore, it is necessary to study the effects of global strain and local distortion on RuO_2.

The origin of the magnetic instability in RuO_2 can be understood from its band structure. The bands near the Fermi level are relatively flat along *Z-R-A-Z* in [Figs. 3(a) and 3(b)]. This flat dispersion gives rise to a large density of states (DOS) near the Fermi energy, making the system more likely to satisfy the generalized Stoner criterion [41]. Also, as ε increases, the susceptibility of RuO_2 gradually increases throughout the reciprocal space (more details are shown in Supplemental Material S9 [31]). These results demonstrate the magnetic instability of RuO_2 under strain conditions from the perspective of band structure.

For the strained RuO_2 system, we can easily notice its altermagnetism, in which the bands are split along *M-G* and *A-Z*, similar to the previous calculations of altermagnetism and the DFT + U calculation results of RuO_2 [42,43]. Moreover, Fig. 3(b) shows the lifting of band degeneracy in other

positions, which correspond to changes of the symmetry of the electronic Hamiltonian during the NM-AFM transition. However, in contrast to the results obtained from DFT + U calculations, the strain-induced RuO_2 altermagnetic spin splitting remains weak at $\varepsilon = 0.8$. In DFT + U calculations, the altermagnetic spin splitting can reach approximately 1 eV along the M–G direction, whereas the strain-induced spin splitting in our calculations is much smaller. The small energy separation between the split bands indicates that the strain-induced magnetic order in RuO_2 does not cause a substantial band renormalization, as shown in Figs. 3(a) and 3(b). Moreover, the Fermi surface of RuO_2 does not undergo a significant reconstruction across the NM–AFM transition. In Figs. 3(c)–3(h), different colors are used to distinguish Fermi-surface sheets originating from different bands. Among these sheets, only the band represented by the red portion exhibits a pronounced modification across the NM–AFM transition, while the band represented by the blue portion changes only slightly. These results indicate that the band structure of strained-induced antiferromagnetic RuO_2 is similar to that of nonmagnetic RuO_2, and therefore does not contradict existing ARPES and quantum oscillation measurements, which indicate the absence of long-range magnetic order in RuO_2 [8–10]. Therefore, the strain-induced magnetic order proposed here may, to some extent, alleviate the concerns raised by band-structure characterizations regarding the existence of magnetic order in RuO_2.

B. The potential SDW state under critical global strain

As studies on the magnetism in RuO_2 have progressed, related work has reported the abnormal GHz-range low-energy excitation in RuO_2/Py thin-film systems and attributed this phenomenon to the existence of SDW in RuO_2 [44]. This excitation differs from the RuO_2 spin wave spectrum predicted in earlier theoretical calculations [4]. In particular, the GHz-range low-energy mode contradicts the THz excitations typically expected for antiferromagnets, revealing the rich antiferromagnetic behavior of RuO_2. Related experiments have also suggested the presence of strain–spin fluctuations in RuO_2 [45]. In fact, SDW ground state in metals is thought to arise as a consequence of electron-electron interaction. This often occurs when the Fermi surface is relatively fragile and sensitive to external perturbations. Although there is no Fermi surface nesting in RuO_2 (Fermi surface nesting is commonly regarded as a favorable condition for SDW formation), the band structure of RuO_2 is unstable. Therefore, lattice local distortion may lead to renormalization of the electronic structure of RuO_2, thereby inducing SDW.

We first discuss the case without local distortion. In the absence of Fermi-surface nesting, the energy of the SDW state is expected to be higher than that of the AFM state when RuO_2 lacks local distortion. To verify this point, we tentatively calculate the energies of the SDW and AFM states in a $16 \times 1 \times 1$ supercell under different values of ε, without introducing any local distortion. The SDW state is constructed by setting a harmonic magnetic-moment distribution as the initial magnetic-moment distribution while ensuring that the magnetic moments of neighboring Ru atoms remained antiparallel. In fact, the SDW state corresponds to a local

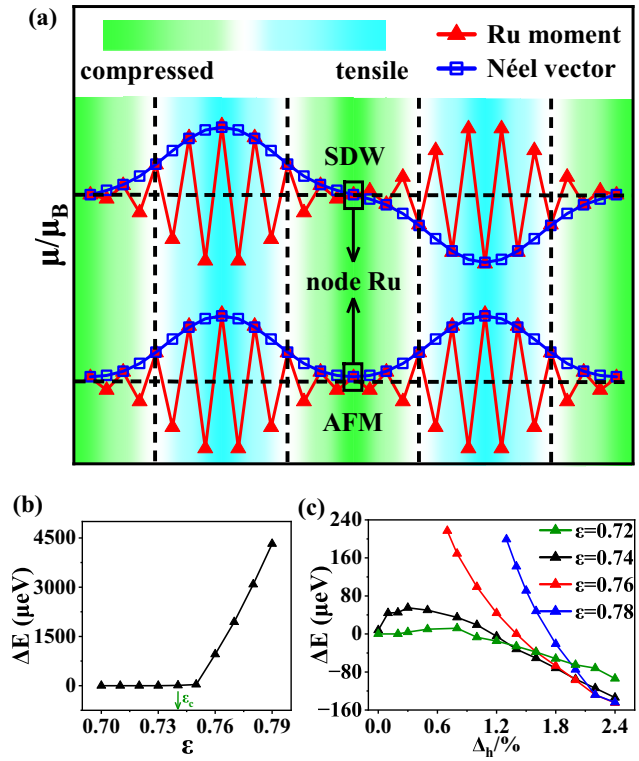

FIG. 4. (a) Schematic diagram of magnetic moment and Néel vector distribution in SDW and amplitude modulated AFM under the harmonic distortion. The Ru atom at the node is node Ru (SDW). The Ru atom which magnetic moment is maximum is $\mu_{\max}$ Ru (SDW). (b) The energy difference between AFM and SDW $\Delta E = E_{\mathrm{SDW}} - E_{\mathrm{AFM}}$ corresponding to different ε when $n = 8$ without considering the local distortion. (c) ΔE corresponding to different Δ_h when $n = 8$, $\varepsilon = 0.72, 0.74, 0.76, 0.78$.

minimum. Therefore, even though the SDW state has a higher energy than the AFM state, the Néel vector will not flip during convergence and thus become the AFM state. In Fig. 4(a), we can find that the difference between AFM and SDW stems from whether the Néel vector changes on both sides of the node. As shown in Fig. 4(b), in the absence of local distortion, the excess energy of the SDW state relative to the AFM state, $\Delta E = E_{\mathrm{SDW}} - E_{\mathrm{AFM}}$, rapidly increases to the meV scale once magnetic order is established. Physically, at the SDW nodes, the Néel vector reverses and the local magnetic moment in the node is strongly suppressed. This suppression produces an exchange-energy penalty, making the SDW a high-energy solution. However, RuO_2 naturally exhibits local distortions in film systems; therefore, the SDW state can be further evaluated by introducing a priori periodic local distortion.

We construct a global strain + local distortion model to investigate how local distortions affect the magnetic order in RuO_2 [Fig. 4(a)]. In the SDW state, the orientation of the Néel vector varies spatially, whereas in the AFM state, its orientation remains constant. By contrast, away from the nodes, the difference in the magnitudes of the magnetic moments between the AFM and SDW states is relatively small. Since the period of the local distortion is half of the SDW period, we need to build a supercell containing two local-distortion

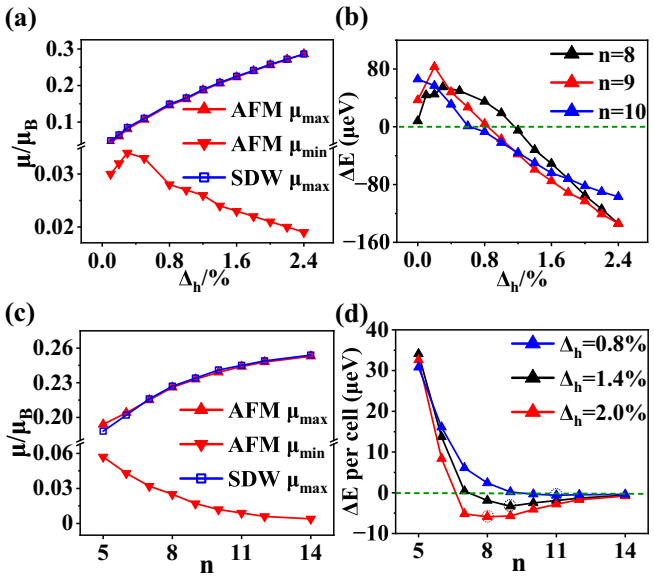

FIG. 5. (a) $\mu_{\max}$ and $\mu_{\min}$ corresponding to different Δ_h when $\varepsilon = \varepsilon_c, n = 8$. (b) ΔE corresponding to different Δ_h when $\varepsilon = \varepsilon_c, n = 8, 9, 10$. (c) $\mu_{\max}$ and $\mu_{\min}$ corresponding to different n when $\varepsilon = \varepsilon_c, \Delta_h = 1.4\%$. (d) ΔE corresponding to different n when $\varepsilon = \varepsilon_c, \Delta_h = 0.8\%, 1.4\%, 2.0\%$.

periods to compute the SDW state. We set n is the local distortion period measured in the number of unit cells. And we construct a $2n \times 1 \times 1$ locally distorted supercell. The lattice constants are defined as follows:

Harmonic distortion:

$$a_i = a_\varepsilon\left(1 - \Delta_h \cos\frac{(2i-1)\pi}{n}\right),$$
$$b = a_\varepsilon, \quad c = c_\varepsilon, \tag{4}$$

here, i is the unit-cell index ($i = 1, 2, \ldots, 2n$), and Δ_h is the amplitude parameter of the local distortion. Based on the model, we can set $n = 8$ as an example at first.

Based on the local distortion introduced,we can calculate ΔE for different Δ_h values [Fig. 4(c)]. When $\varepsilon > \varepsilon_c$, ΔE decreases as Δ_h increases, but to achieve $\Delta E < 0$, the required Δ_h becomes larger as ε increases. When $\varepsilon < \varepsilon_c$, the global magnetic order is more difficult to establish, making the emergence of the SDW state more challenging. Notably, when $\varepsilon \approx \varepsilon_c$, ΔE exhibits a nonmonotonic dependence on Δ_h, first increasing and then decreasing, and the SDW becomes the ground state for $\Delta_h > 1.2\%$. Since local distortions on the order of 1% are fairly common in epitaxial RuO_2 thin film, SDW is more likely to become a potential ground state near ε_c. But when ε is far away from ε_c, the system stays NM or AFM.

To clarify why local distortions can render the SDW state a potential ground state, we evaluate the dependence of ΔE, $\mu_{\max}$, $\mu_{\min}$ on Δ_h when $\varepsilon = \varepsilon_c$ (the magnetic moment spatial distributions are provided in Supplemental Material S4 [31]) [Fig. 5(a)]. We notice that $\mu_{\max}$ in AFM and SDW is almost identical, indicating that there is little difference between AFM and SDW in the tensile region and thus contribute little to ΔE. By contrast, $\mu_{\min}$ in the AFM state decreases with increasing Δ_h when $\Delta_h > 0.5\%$, implying that the moments in the node regions are continuously suppressed but remain finite, in contrast to the SDW state where the moment at the node is naturally zero. The reason why AFM and SDW nodes exhibit different magnetic orders in the node region is that the Néel vector directions are opposite on both sides of the node in SDW, while the Néel vector direction is consistent in AFM. Since the nodes exhibit the largest difference in absolute moment magnitudes between AFM and SDW, we suggest that they make the dominant contribution to ΔE. So, the physical picture can be described as follows: As Δ_h increases, the suppression of $\mu_{\min}$ by the compressed region is enhanced in AFM. Based on previous calculations, the nodes tend to be nonmagnetic because of the compression. However, due to the antiferromagnetic nonlocality, the node regions still possess a little magnetic order. Therefore, AFM suffers an energy penalty at the nodes (node-energy penalty). In contrast, the nodes in SDW are naturally nonmagnetic, so SDW gains an energy advantage relative to AFM, thus making ΔE more likely to become negative. This behavior remains unchanged in different periods n [Fig. 5(b)], demonstrating the universality of the conclusions that the difference of the magnetism in the node region contributes mainly to the node-energy penalty, thereby changing the specific value of ΔE. This result also holds true under the slab model (more details are provided in Supplemental Material S6 [31]).

To further discuss the importance of node region in SDW formation, we calculated the variations of ΔE per cell (ΔE per cell for different periods is easy to discuss), $\mu_{\max}$, $\mu_{\min}$ with n at different Δ_h values under $\varepsilon = \varepsilon_c$. The results show that $\mu_{\min}$ in AFM decreases rapidly with increasing n [Fig. 5(c)], and ΔE per cell first decreases and then increases with n [Fig. 5(d)]. The physical picture can be understood as follows: As the period n increases from small values, the wavelength of SDW becomes longer, which reduces the exchange-energy penalty and makes SDW more likely to become the ground state. However, as n increases further, the width of the compressed region gradually exceeds the scope of influence of the antiferromagnetic nonlocality. It reduces the influence of the antiferromagnetic nonlocality in the compressed region (the node), which leads to a decrease in the node-energy penalty. In fact, the less node-energy penalty from the antiferromagnetic nonlocality, the less difference the compressed region can feel between AFM and SDW, thus making ΔE per cell approach zero. We further observe that the smaller the distortion amplitude, the longer the wavelength required for the most stable SDW. When $\Delta_h = 0.8\%, 1.4\%, 2.0\%$, the minimum of ΔE per cell occurs at $n = 11, 9, 8$, respectively [Fig. 5(d)], and these Δ_h values are on the order of the experimental situations [21,46] (experimentally, the lattice constant fluctuates between 1% and 3%). This also implies that the characteristic SDW wavelength is 16–22 times the lattice constant a, corresponding to approximately 7–10 nm.

Based on the above discussion, we conclude that the variation in ΔE arises from the competition between the node-energy penalty and the exchange-energy penalty. The node-energy penalty originates from antiferromagnetic nonlocality in RuO_2, whereas the exchange-energy penalty is associated with the reversal of the Néel vector in the

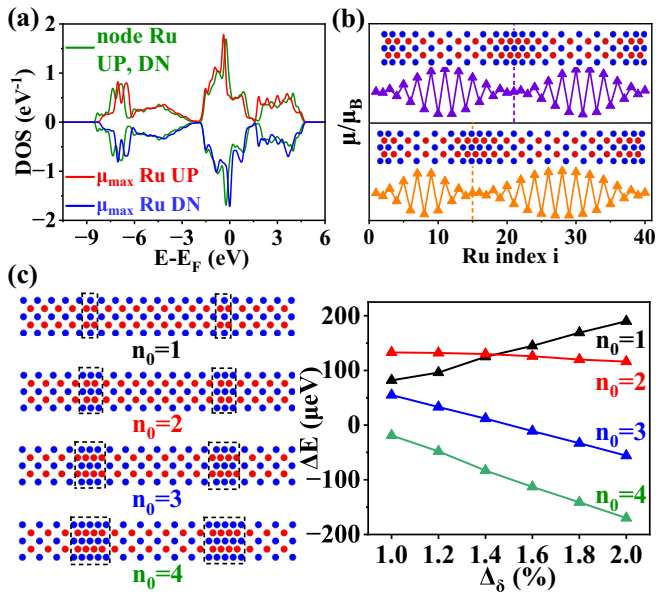

FIG. 6. (a) Ru-projected DOS of $\mu_{\max}$ Ru and node Ru [defined in Fig. 4(a)] in the SDW state with $\varepsilon = \varepsilon_c$, $\Delta_h = 2.4\%$ and $n = 8$. (b) Variation of node position with compressed center when $\varepsilon = \varepsilon_c$, $\Delta_h = 1.0\%$, $n = 10$. (A RuO_2 unit cell has two Ru atoms, so the number of the Ru index is twice the number of the number of the unit cell index.) (c) Schematic diagram of δ–type distortion of RuO_2 and the variation of ΔE with Δ_δ for different n_0 when $\varepsilon = \varepsilon_c$, $n = 10$.

SDW state. From the variation in ΔE shown in Fig. 5(b), we estimate that both penalties are on the order of 100 μeV in a $16 \times 1 \times 1$ supercell, corresponding to approximately 10 μeV per unit cell. In Supplemental Material S7 [31], we present a semiquantitative method for calculating the exchange-penalty energy and the node-penalty energy.

We further analyze the DOS within the local-distortion model. Taking the harmonic distortion with $n = 8$, $\Delta_h = 2.4\%$, and $\varepsilon = \varepsilon_c$ as an example, we compare the difference of Ru-projected DOS between $\mu_{\max}$ Ru and node Ru [defined in Fig. 4(a)] in SDW [Fig. 6(a)]. We notice that $\mu_{\max}$ Ru exhibits a slight spin-splitting feature compared to node Ru, which indicates the weak magnetic order in RuO_2 compared to DFT + U calculation results.

These results in Fig. 4(c) suggest that, within an idealized model with periodic distortions, the SDW state can emerge as a potential ground state in RuO_2. In realistic thin film systems, there is no local distortion period, and the magnetic moment distribution of SDW is expected to be adjusted accordingly. Therefore, we construct a class of local-distortion models in which the position of the compressed region can be tuned. In this way, we can control the pinning position of SDW nodes to simulate the realistic condition (see Supplemental Material S5 [31] for details). Our calculations show that the SDW node is pinned in the center of the most compressed region and follows the motion of the compressed region [Fig. 6(b)]. This result demonstrates that the node position responds to local distortions and implies that the SDW wavelength in RuO_2 is not a strictly unique constant, but is closely tied to the characteristic length scale of the local distortion.

In practice, many extrinsic factors such as defects, interface steps, and local relaxation can provide local distortions, which are usually limited to nanoscale regions. To capture this strong distortion in a finite spatial extent, we introduce a more realistic δ-distortion model to simulate the realistic situation. The lattice distortion is defined as

δ–type distortion:

$$a_i = \begin{cases} a_\varepsilon(1-\Delta_\delta) & 1 \leqslant i \leqslant n_0 \quad \text{or} \quad n+1 \leqslant i \leqslant n+n_0 \\ a_\varepsilon\left(1+\frac{n_0}{n-n_0}\Delta_\delta\right) & \text{otherwise,} \end{cases}$$

$$b = a_\varepsilon, \quad c = c_\varepsilon. \tag{5}$$

Here n_0 denotes the number of compressed unit cells within each local-distortion period, while $n - n_0$ corresponds to the number of tensile unit cells within each local-distortion period. This construction ensures $\langle a_i \rangle = a_\varepsilon$ over one period and is closer to the thin-film reality of strong distortion in a finite spatial extent.

To examine the impact of strong distortion in a finite spatial extent on RuO_2 magnetic order, we set $n = 10$ and $\varepsilon = \varepsilon_c$ and construct a $20 \times 1 \times 1$ locally distorted supercell. We can tune the width of the compressed region by varying n_0 [Fig. 6(c)]. The results show that for $n_0 = 1$, ΔE increases with increasing Δ_δ; for $n_0 = 2, 3, 4$, ΔE decrease linearly with increasing Δ_δ, while the slope decreases as n_0 becomes larger. This behavior indicates that stabilizing SDW relative to AFM requires a sufficiently extended locally compressed region. It also implies that the specific value of ΔE is closely linked to the local compressed condition in the film, consistent with the trend obtained from the harmonic distortion analysis.

Combining the above results, we can arrive at two conclusions and summarize this section:

(1) Local distortions near the critical global strain can stabilize a SDW ground state in RuO_2. In this system, the energy competition between AFM and SDW comes from the competition between the node-energy penalty and the exchange-energy penalty, and the energy competition is governed primarily by local-compression environment. Enhanced compression at the nodes increases the node-energy penalty of AFM over SDW. As the spatial extent of the compressed region increases, ΔE can exhibit a nonmonotonic behavior, i.e., first decreases and then rises again.

(2) The characteristic SDW wavelength in RuO_2 is set by the distortion strength. A distortion length of approximately 7–10 nm is most favorable for stabilizing SDW. If the distortion length is shorter, exchange-energy penalty will increase rapidly, making SDW less competitive. If the distortion length is longer, the energy difference between AFM and SDW decreases and the two states approach near degeneracy.

However, which state is the ground state is not important in reality, because the energy difference is so small ($\approx$1 K) that it is unlikely to significantly affect the population of the system. Indeed, such a small energy scale suggests that quantum and thermal fluctuations may prevent SDW from developing long-range order. Since the only difference between SDW and AFM is whether the Néel vectors on both sides of the node are opposite, and the local distortion distribution in space is also random, we propose that in real systems, SDW may behave as antiferromagnetic domain walls, and their distribution range may be as wide as that of such domain walls [32]. Meanwhile,

ΔE is comparable to microwave energy scales, with 1 GHz corresponding to approximately 4 μeV. Therefore, the present calculations provide useful insights into the low-energy magnetic excitations observed in RuO_2, which is far lower than the THz-scale magnon energies typical of conventional antiferromagnets.

IV. CONCLUSIONS

In this work, we investigate the extrinsic magnetic order in RuO_2 by analyzing the effects of global strain and local distortions. When the global strain on RuO_2 reaches a certain level, RuO_2 undergoes a transition from a nonmagnetic state to an antiferromagnetic state. Near the NM–AFM critical strain, introducing a modest local distortion can render a SDW state energetically competitive and potentially stabilize SDW as the ground state. The energy difference between SDW and AFM depends on both the characteristic length scale and the amplitude of the local distortion. In particular, when the compressed region extends over several lattice constants and the distortion amplitude reaches the 1% level, SDW can become the ground state.

Given the pronounced sensitivity of RuO_2 to both global strain and local distortions, the mechanism identified here has several implications. First, the results provide a unified framework for rationalizing the discrepancies on different substrates and epitaxial orientations, where the global strain vary substantially. Second, the result highlights the potential influence of local distortion on RuO_2 thin films, which means that the magnetic order in RuO_2 will undergo subtle changes under different morphologies and interface environments. Finally, the results suggest an additional route for controlling spin transport in RuO_2, offering computational support for strain-based tuning and expanding the strain-tuning dimension available for spintronic devices.

ACKNOWLEDGMENTS

This work is supported by the National Natural Science Foundation of China (Grants No. 52171231 and No. 123B2054), the Fund of National Key Laboratory on Vacuum Technology and Physics (No. 61422072306), 111 Center (Grant No. B20063) and Supercomputing Center of Lanzhou University.

DATA AVAILABILITY

The data that support the findings of this article are openly available [47].

[1] L. Šmejkal, J. Sinova, and T. Jungwirth, Emerging research landscape of altermagnetism, Phys. Rev. X **12**, 040501 (2022).

[2] T. Berlijn, P. C. Snijders, O. Delaire, H.-D. Zhou, T. A. Maier, H.-B. Cao, S.-X. Chi, M. Matsuda, Y. Wang, M. R. Koehler, P. R. C. Kent, and H. H. Weitering, Itinerant antiferromagnetism in RuO_2, Phys. Rev. Lett. **118**, 077201 (2017).

[3] K.-H. Ahn, A. Hariki, K.-W. Lee, and J. Kuneš, Antiferromagnetism in RuO_2 as d-wave Pomeranchuk instability, Phys. Rev. B **99**, 184432 (2019).

[4] L. Šmejkal, A. Marmodoro, K.-H. Ahn, R. González-Hernández, I. Turek, S. Mankovsky, H. Ebert, S. W. D'Souza, O. Šipr, J. Sinova, and T. Jungwirth, Chiral magnons in altermagnetic RuO_2, Phys. Rev. Lett. **131**, 256703 (2023).

[5] H. Bai, Y. C. Zhang, Y. J. Zhou, P. Chen, C. H. Wan, L. Han, W. X. Zhu, S. X. Liang, Y. C. Su, X. F. Han, F. Pan, and C. Song, Efficient spin-to-charge conversion via altermagnetic spin splitting effect in antiferromagnet RuO_2, Phys. Rev. Lett. **130**, 216701 (2023).

[6] M. Hiraishi, H. Okabe, A. Koda, R. Kadono, T. Muroi, D. Hirai, and Z. Hiroi, Nonmagnetic ground state in RuO_2 revealed by muon spin rotation, Phys. Rev. Lett. **132**, 166702 (2024).

[7] P. Keßler, L. Garcia-Gassull, A. Suter, T. Prokscha, Z. Salman, D. Khalyavin, P. Manuel, F. Orlandi, I. I. Mazin, R. Valentí, and S. Moser, Absence of magnetic order in RuO_2: Insights from μSR spectroscopy and neutron diffraction, npj Spintron. **2**, 50 (2024).

[8] J. Liu, J. Zhan, T. Li, J. Liu, S. Cheng, Y. Shi, L. Deng, M. Zhang, C. Li, J. Ding, Q. Jiang, M. Ye, Z. Liu, Z. Jiang, S. Wang, Q. Li, Y. Xie, Y. Wang, S. Qiao, J. Wen, *et al.*, Absence of altermagnetic spin splitting character in rutile oxide RuO_2, Phys. Rev. Lett. **133**, 176401 (2024).

[9] T. Osumi, K. Yamauchi, S. Souma, P. Shubhankar, A. Honma, K. Nakayama, K. Ozawa, M. Kitamura, K. Horiba, H. Kumigashira, C. Bigi, F. Bertran, T. Oguchi, T. Takahashi, Y. Maeno, and T. Sato, Spin-degenerate bulk bands and topological surface states of RuO_2 Phys. Rev. B **113**, 085116 (2026).

[10] Z. Wu, M. Long, H. Chen, S. Paul, H. Matsuki, O. Zheliuk, U. Zeitler, G. Li, R. Zhou, Z. Zhu, D. Graf, T. I. Weinberger, F. M. Grosche, Y. Maeno, and A. G. Eaton, Fermi surface of RuO_2 measured by quantum oscillations, Phys. Rev. X **15**, 031044 (2025).

[11] A. Smolyanyuk, I. I. Mazin, L. Garcia-Gassull, and R. Valentí, Fragility of the magnetic order in the prototypical altermagnet RuO_2, Phys. Rev. B **109**, 134424 (2024).

[12] Z. Qian, Y. Yang, S. Liu, and C. Wu, Fragile unconventional magnetism in RuO_2 by proximity to Landau-Pomeranchuk instability, Phys. Rev. B **111**, 174425 (2025).

[13] S. G. Jeong, S. Lee, B. Lin, Z. Yang, I. H. Choi, J. Y. Oh, S. Song, S. wook Lee, S. Nair, R. Choudhary, J. Parikh, S. Park, W. S. Choi, J. S. Lee, J. M. LeBeau, T. Low, and B. Jalan, Metallicity and anomalous Hall effect in epitaxially strained, atomically thin RuO_2 films, Proc. Natl. Acad. Sci. USA **122**, e2500831122 (2025).

[14] D. Q. Ho, D. Q. To, R. Hu, G. W. Bryant, and A. Janotti, Symmetry-breaking induced surface magnetization in nonmagnetic RuO_2, Phys. Rev. Mater. **9**, 094406 (2025).

[15] L. Šmejkal, R. González-Hernández, T. Jungwirth, and J. Sinova, Crystal time-reversal symmetry breaking and spontaneous Hall effect in collinear antiferromagnets, Sci. Adv. **6**, eaaz8809 (2020).

[16] K. Tanaka, T. Nomoto, and R. Arita, First-principles study of the tunnel magnetoresistance effect with Cr-doped RuO_2 electrode, Phys. Rev. B **110**, 064433 (2024).

[17] Y. Q. Liu, M. S. Si, G. P. Zhang, H. Du, and Z. M. Zhang, Anisotropic high harmonic generation as a gauge of altermagnetism in RuO_2, Phys. Rev. B **112**, L081105 (2025).

[18] S. G. Jeong, B. Y. X. Lin, M. Jin, I. H. Choi, S. Lee, Z. Yang, S. Nair, R. Choudhary, J. Parikh, A. Santhosh, M. Neurock, K. A. Stoerzinger, J. S. Lee, T. Low, Q. Tu, J. M. LeBeau, and B. Jalan, Strain-stabilized interfacial polarization tunes work function over 1 eV in RuO_2/TiO_2 heterostructures, Nat. Commun. **17**, 2516 (2026).

[19] A. Akashdeep, S. Krishnia, J.-H. Ha, S. An, M. Gaerner, T. Prokscha, A. Suter, G. Janka, G. Reiss, T. Kuschel, D.-S. Han, A. D. Bernardo, Z. Salman, G. Jakob, and M. Kläui, Surface-localized magnetic order in RuO_2 thin films revealed by low-energy muon probes Appl. Phys. Lett. **128**, 022406 (2026).

[20] A. K. Rajapitamahuni, S. Nair, Z. Yang, A. K. Manjeshwar, S. G. Jeong, W. Nunn, and B. Jalan, Thickness-dependent insulator-to-metal transition in epitaxial RuO_2, Phys. Rev. Mater. **8**, 075002 (2024).

[21] J. D. S. Forte, S. G. Jeong, A. Santhosh, S. Lee, B. Jalan, and T. Low, Strain engineering of altermagnetic symmetry in epitaxial RuO_2 films, Phys. Rev. B **114**, 084408 (2026).

[22] S. G. Jeong, I. H. Choi, S. Lee, J. Y. Oh, S. Nair, J. H. Lee, C. Kim, A. Seo, W. S. Choi, T. Low, J. S. Lee, and B. Jalan, Anisotropic strain relaxation-induced directional ultrafast carrier dynamics in RuO_2 films, Sci. Adv. **11**, eadw7125 (2025).

[23] F. Liu, Y. Song, Z. Zhang, Y. Liu, S. Zhu, Z. Lu, and R. Xiong, Strain-induced non-alter compensated magnet and its application to magnetic tunnel junction device design, arXiv:2506.22770.

[24] D. Sander, The magnetic anisotropy and spin reorientation of nanostructures and nanoscale films, J. Phys.: Condens. Matter **16**, R603 (2004).

[25] P. Hohenberg and W. Kohn, Inhomogeneous electron gas, Phys. Rev. **136**, B864 (1964).

[26] W. Kohn and L. J. Sham, Self-consistent equations including exchange and correlation effects, Phys. Rev. **140**, A1133 (1965).

[27] P. E. Blöchl, Projector augmented-wave method, Phys. Rev. B **50**, 17953 (1994).

[28] G. Kresse and D. Joubert, From ultrasoft pseudopotentials to the projector augmented-wave method, Phys. Rev. B **59**, 1758 (1999).

[29] G. Kresse and J. Furthmüller, Efficiency of *ab-initio* total energy calculations for metals and semiconductors using a plane-wave basis set, Comput. Mater. Sci. **6**, 15 (1996).

[30] G. Kresse and J. Furthmüller, Efficient iterative schemes for *ab initio* total-energy calculations using a plane-wave basis set, Phys. Rev. B **54**, 11169 (1996).

[31] See Supplemental Material at http://link.aps.org/supplemental/10.1103/4gky-vck5 for the discussion of computational details, rigor, and universality (S1, S5–S10), supplemental data of concern to peers (S2, S3) and supplemental figures for the article's visualization (S4).

[32] Y. Hu, X. Wang, C. Chen, Q. Zhang, D. Zhao, T. Zhang, C. Wang, Q.-H. Wang, D. Feng, and T. Zhang, Discovery of itinerant magnetic domain wall and quasiparticle boundary state in spin-density-waves, arXiv:2402.15999.

[33] V. Wang, N. Xu, J.-C. Liu, G. Tang, and W.-T. Geng, VASPKIT: A user-friendly interface facilitating high-throughput computing and analysis using VASP code, Comput. Phys. Commun. **267**, 108033 (2021).

[34] K. Momma and F. Izumi, *VESTA3* for three-dimensional visualization of crystal, volumetric and morphology data, J. Appl. Crystallogr. **44**, 1272 (2011).

[35] Y.-C. Zhang, H. Bai, D.-H. Zhang, C. Chen, L. Han, S.-X. Liang, R.-Y. Chu, J.-K. Dai, M. Sawicki, F. Pan, and C. Song, Probing the Néel order in altermagnetic RuO_2 films via x-ray magnetic linear dichroism, Chin. Phys. Lett. **42**, 027301 (2025).

[36] M. Alaei, N. Rezaei, I. Mikhailov, A. R. Oganov, and A. Qaiumzadeh, Complex magnetic behavior in RuO_2 thin films driven by strain and substrate effects (unpublished).

[37] M. Uchida, T. Nomoto, M. Musashi, R. Arita, and M. Kawasaki, Superconductivity in uniquely strained, Phys. Rev. Lett. **125**, 147001 (2020).

[38] J. P. Ruf, H. Paik, N. J. Schreiber, H. P. Nair, L. Miao, J. K. Kawasaki, J. N. Nelson, B. D. Faeth, Y. Lee, B. H. Goodge, B. Pamuk, C. J. Fennie, L. F. Kourkoutis, D. G. Schlom, and K. M. Shen, Strain-stabilized superconductivity, Nat. Commun. **12**, 59 (2021).

[39] B. Z. Gregory, N. Wadehra, S. Zhang, Y. Wu, S. Poage, J. Strempfer, A. K. Kundu, A. Rajapitamahuni, E. Vescovo, A. Verma, B. Pamuk, J. Ruf, H. Nair, N. J. Schreiber, K. Ahadi, K. M. Shen, D. G. Schlom, and A. Singer, Resonant diffraction and photoemission inconsistent with altermagnetism in epitaxial RuO_2 films, arXiv:2510.13781.

[40] N. Wadehra, B. Z. Gregory, S. Zhang, N. Schnitzer, Y. Iguchi, Y. E. Li, B. Pamuk, D. A. Muller, A. Singer, K. M. Shen, and D. G. Schlom, Strain-induced superconductivity in RuO_2(100) thin-films, Commun. Mater. **6**, 135 (2025).

[41] Y.-F. Hou, J. Lu, X. Chen, G.-B. Liu, and P. Zhang, Nonmagnetic-magnetic transitions in rutile RuO_2, arXiv:2604.14764.

[42] D.-F. Shao, S.-H. Zhang, M. Li, C.-B. Eom, and E. Y. Tsymbal, Spin-neutral currents for spintronics, Nat. Commun. **12**, 7061 (2021).

[43] Y. Noda, K. Ohno, and S. Nakamura, Momentum-dependent band spin splitting in semiconducting MnO_2: A density functional calculation, Phys. Chem. Chem. Phys. **18**, 13294 (2016).

[44] X. Feng, H. Bai, X. Fan, M. Guo, Z. Zhang, G. Chai, T. Wang, D. Xue, C. Song, and X. Fan, Incommensurate spin density wave in antiferromagnetic RuO_2 evinced by abnormal spin splitting torque, Phys. Rev. Lett. **132**, 086701 (2024).

[45] I. H. Choi, S. G. Jeong2, J. H. Lee, S. Kang, S. Nair, C. Kim, D. Wulferding, B. Jalan, and J. S. Lee, Strain-induced dynamic spin-phonon coupling in epitaxial RuO_2 films, arXiv:2509.23969.

[46] B. Z. Gregory, N. Wadehra, S. Zhang, Y. Wu, S. Poage, J. Strempfer, A. K. Kundu, A. Rajapitamahuni, E. Vescovo, A. Verma, B. Pamuk, J. Ruf, H. Nair, N. J. Schreiber, K. Ahadi, K. M. Shen, D. G. Schlom, and A. Singer, Resonant diffraction and photoemission inconsistent with altermagnetism in epitaxial RuO_2 films, arXiv:2510.13781.

[47] Lanzhou University, The data for the article "Strain-induced magnetic order in RuO2 from first pricinples calculations", Zenodo, 2026, https://doi.org/10.5281/zenodo.22077956.